Lightwave valleytronics in a monolayer of tungsten diselenide

F. Langer[#1], **C. P. Schmid**[1], **S. Schlauderer**[1], **M. Gmitra**[1], **J. Fabian**[1], **P. Nagler**[1], **C. Schüller**[1], **T. Korn**[1], **P. G. Hawkins**[#2], **J. T. Steiner**[2], **U. Huttner**[2], **S. W. Koch**[2], **M. Kira**[3,+], and **R. Huber**[1]

[1]Department of Physics, University of Regensburg, 93040 Regensburg, Germany

[2]Department of Physics, University of Marburg, 35032 Marburg, Germany

[3]Department of Electrical Engineering and Computer Science, University of Michigan, Ann Arbor, Michigan 48109, USA

[#] These authors contributed equally to this work.

Abstract

As conventional electronics is approaching its ultimate limits1, nanoscience has urgently sought for novel fast control concepts of electrons at the fundamental quantum level2. Lightwave electronics3 – the foundation of attosecond science4 – utilizes the oscillating carrier wave of intense light pulses to control the translational motion of the electron's charge faster than a single cycle of light5–15. Despite being particularly promising information carriers, the internal quantum attributes of spin16 and valley pseudospin17–19 have not been switchable on the subcycle scale20–21. Here we demonstrate lightwave-driven changes of the valley pseudospin and introduce distinct signatures in the optical read out. Photogenerated electron–hole pairs in a monolayer of tungsten diselenide are accelerated and collided by a strong lightwave. The emergence of high odd-order sidebands and anomalous changes in their polarization direction directly attest to the ultrafast pseudospin dynamics. Quantitative computations combining density-functional theory with a non-perturbative quantum many-body approach assign the polarization of the sidebands to a lightwave-induced change of the valley pseudospin and confirm that the process is coherent and adiabatic. Our work opens the door to systematic valleytronic logic at optical clock rates.

In a crystalline solid, a set of atoms forming the unit cell repeats itself on a periodic lattice. The Bloch theorem22 states that a single-electron wave function $\phi_{\alpha\mathbf{k}}$, is composed of a plane wave with wave vector $\mathbf{k}$ and a lattice periodic part $u_{\alpha\mathbf{k}}$:

$$\phi_{\alpha\mathbf{k}}(\mathbf{r}) = u_{\alpha\mathbf{k}}(\mathbf{r})\exp(i\mathbf{k} \cdot \mathbf{r}). \quad (1)$$

The plane-wave part describes the effective motion of electrons throughout the crystal whereas $u_{\alpha\mathbf{k}}(\mathbf{r})$ encodes the contribution from atomic orbitals and spins (quantum number α). In conventional electronics, quasi-static fields cause a tiny imbalance of the number of electrons moving in $+\mathbf{k}$ and $-\mathbf{k}$ directions. This leads to incoherent charge currents. In quantum electronics, in contrast, one tries to coherently transport the quantum information stored in atomic orbitals or spins before coherence-destroying scattering becomes effective[23]. Recently, the carrier wave of intense light pulses has been exploited as an AC bias to transport electrons faster than scattering occurs, yielding intriguing quantum effects such as dynamical Bloch oscillations[5,7,11,13], electron–hole recollisions[6,12,24], electronic quantum interference[8,9], and interband excitations[8–10]. The resulting high-harmonic radiation[5,7,8,10–15] has been used to retrieve the electronic bandstructure[25], all optically. Despite the first evidence of Berry's phase effects[13,26], resulting directly from the topological $\mathbf{k}$ dependence of $u_{\alpha\mathbf{k}}$, most lightwave-driven transport of electric charge has focused on controlling $\mathbf{k}$ in the plane-wave part of the Bloch wave function.

Independently, quantum information processing[2] has been pursued using internal degrees of freedom encoded in $u_{\alpha\mathbf{k}}$, such as spin[16] or valley pseudospin[17–21,27–30]. Monolayers of transition metal dichalcogenides (TMDCs) form an ideal testbed for such concepts because they feature two separate band minima – called valleys[17–19] – that can be selectively excited by optical means[18,19,27–29]. The coherence of the valley pseudospin has been shown to be conserved even in steady-state photoluminescence experiments[27–29], rendering this degree of freedom a promising information carrier[17–19,21,27–30]. Yet, its subcycle manipulation remains an open challenge.

Here, we demonstrate that the valley pseudospin in a TMDC monolayer can be changed by lightwave-driven intraband transport within few femtoseconds. To this end, we accelerate optically prepared coherent electron–hole pairs in monolayer tungsten diselenide (WSe_2) by intense, phase-stable multi-terahertz (THz) waveforms[12]. Recolliding electrons and holes emit their kinetic energy in high-order sidebands, the odd orders of which directly reflect the electron–hole pair's valley pseudospin. Pairs that are selectively created in a single valley can be transferred partly into the opposite valley by the strong THz field, leaving a unique fingerprint in elliptically polarized sidebands.

Monolayers of WSe_2 (Fig. 1a) feature an electronic band structure with a direct energy gap separating the filled valence band from the empty conduction band at the corners of the hexagonal unit cell in momentum space, called the Brillouin zone[17–19] (Fig. 1b). Owing to the honeycomb crystal lattice (Fig. 1a), the Brillouin zone contains two inequivalent corners[17–19] – the K and the K' points. In the vicinity of K (K'), the electronic wave function $u_{\alpha\mathbf{k}}$ of the highest valence band is primarily composed of atomic $5d$ orbitals of tungsten with a magnetic quantum number $m = 2$ (–2) (refs. 18,19). A sign flip of m implies a time inversion of the electronic wave function $u_{\alpha\mathbf{k}}$ between K and K' (insets in Fig. 1b). Also the conduction band wave functions at the K and K' points are time-reversal pairs. This

is why circularly polarized light can prepare electron–hole pairs selectively at the K or the K' point, depending on helicity[17–21,27–29], and the valley polarization may be described by a spin-like quantity called valley pseudospin. In the following, we determine whether intense THz pulses can drive electron transport far enough to induce superpositions of K and K' states and to ultimately flip the valley pseudospin.

We start with a linearly polarized 100-fs near-infrared pulse to create electron–hole pairs in bulk and monolayer WSe_2 on a diamond substrate (Extended Data Figure 1). Being a superposition of right- (σ_+) and left-circularly (σ_-) polarized light, this preparation pulse generates coherent electron–hole pairs in both the K and K' valleys. Coulomb attraction causes the quasiparticles to form a series of atom-like bound states, called excitons[23]. Our preparation pulse is resonant with the 1s A exciton[12,17–20] (photon energy, 1.621 eV for the bulk and 1.665 eV for the monolayer). Simultaneously, an intense THz transient (inset in Fig. 1c; centre frequency, $\nu_{THz} = 40$ THz) coherently drives the excitonic polarization leading to real-space acceleration followed by a recollision of the constituent electron and hole. These dynamics are reminiscent of the three-step model underlying attosecond pulse generation in atomic gases[4]. Upon recollision, the electron can recombine with the hole, while it emits a photon with an energy corresponding to the bandgap plus the kinetic energy imparted by the acceleration.

In bulk WSe_2, this mechanism leads to the generation of high-order sidebands accompanying the interband 1s exciton line (Fig. 1c, black curve). Since the bulk crystal is inversion symmetric, high-order sideband generation (HSG) is independent of the polarity of the driving field, and collisions between the excitonic constituents occur in every half cycle. In the frequency domain, this periodicity causes even sideband orders with a spectral separation of $2\nu_{THz}$.

Figure 1c also depicts the first high-order sideband emission from a monolayer material (red curve). Despite the ultimately low sample thickness, harmonic sidebands up to order $n = 11$ clearly rise above the noise floor. Remarkably, the sideband spectrum differs qualitatively from the bulk case. Besides even orders, we also detect odd orders (n > 3) of comparable strength – a result that has neither been predicted nor observed before. Phenomenologically, the emergence of HSG spaced by ν_{THz} implies that the time structure of the light emission is periodic after a full oscillation cycle of the THz wave, that is, it differs for positive and negative THz half cycles.

For a microscopic understanding, we first note that the strongest odd-order sideband intensity occurs when electron–hole pairs are accelerated along the zigzag crystal direction (Fig. 1c, red curve), whereas HSG is strongly suppressed for THz fields along the armchair direction (Fig. 1c, blue curve). Since inversion symmetry along the zigzag direction is broken only in momentum space (Fig. 1b, red arrow), not in real space (Fig. 1a, red arrow), our observation proves that odd-order sideband generation must be related to intraband transport, best understood in momentum space. The THz field drives electrons and holes within the bands, in which the near-infrared pulse has prepared them. The emergence of odd-order HSG indicates that the coherent electron–hole pairs traverse a large fraction of the Brillouin zone to reach wave vectors $\mathbf{k}$ at which the effective mass is no longer isotropic.

Hence, the carrier dynamics depend on the sign of the driving waveform and a spectral modulation of the sideband radiation with ν_{THz} results.

We corroborate this conjecture by computing the full band structure of the WSe_2 monolayer with density functional theory (DFT, see Methods). For large excursions from the K or K' points, the electron–hole pairs do indeed experience strong asymmetries of the band structure along the zigzag direction (Fig. 2a). In contrast, the band structure in the armchair direction is symmetric about the K and the K' points (Fig. 2b). Consequently, the sideband spectrum is expected to show barely any odd orders, as indeed observed in Fig. 1c.

Nevertheless, this explanation is incomplete because the linearly polarized preparation pulse populates both K and K' valleys equally. Since the bands in these valleys are mirror images of each other (see Fig. 2a) the plane-wave part of the electron–hole dynamics of the ensemble is effectively symmetric for positive and negative THz half cycles, which forbids generation of odd-order sidebands. This obvious contradiction with the experiment can be resolved only if the valley pseudospin, encoded in the atomic wave function $u_{\alpha,k}$, is taken into account. Therefore, we simulate the entire life cycle of the electron–hole pairs by combining a DFT calculation of the electronic band structure and the Bloch states with cluster expansion23 (CE) to solve the lightwave-driven non-perturbative many-body dynamics. We quantitatively include the electron–hole Coulomb interaction, pseudospin, and dipole-matrix elements in two-dimensional computations for conditions matching the experiment (see Methods).

The computed high-order sideband spectra (Fig. 2c) reproduce the experimental results very well, including the emergence of even and odd orders as well as details, such as the suppression of the third-order sideband (see Methods). Most importantly, the presence of odd-order sidebands is observable in our setting only if the valley pseudospin is accounted for. The different pseudospin in the K and K' valleys imparts different helicities on the sideband radiation resulting from recombination within the respective valleys. This fact breaks the symmetry for positive and negative THz field polarities and enables the generation of odd orders. Interestingly, the pseudospin tagging of the K and K' excitations causes a characteristic polarization state of the sidebands (Figs. 3a and b). Straightforward vector algebra (see Methods) shows that summing up the counter-circularly rotating field vectors of odd-order sidebands from the K and K' valleys yields a field that is linearly polarized perpendicular to the excitation pulse. Analogously, one can show that even-order sidebands have to be polarized parallel with the excitation light.

We test this prediction by measuring the intensity of even and odd sideband orders with an analyser set at angle θ (Figs. 3c and d). Here $\theta = 0°$ (90°) denotes a polarization parallel (perpendicular) to the near-infrared and the THz fields. As expected in the zigzag direction, even-order sidebands are indeed polarized parallel to the excitation light, while odd orders are perpendicularly polarized (Figs. 3a and c). By crystal symmetry, the armchair direction supports only even orders, which are polarized at $\theta = 0°$ (Figs. 3b and d). This theory–experiment comparison further corroborates that odd-order HSG is a fingerprint of the valley coherence, which prevails even under atomically strong fields.

To trace precisely how the THz field changes the valley pseudospin, we selectively excite the K valley by a σ_+ polarized excitation pulse. If the electron–hole pairs recollide within the same valley, their sideband emission is expected to remain polarized with the same helicity. Figure 4a shows the σ_+ polarization of the near-infrared preparation pulse (black curve) as well as the polarization state of the sideband orders $n = 4$ to 7, recorded by measuring the intensity as a function of the angle of a rotating analyser. In stark contrast to the incident pulse, the sidebands are polarized strongly elliptically, with their principal axis aligned at a large angle θ (Fig. 4a). Our many-body computations (Fig. 4b) produce essentially the same polarization and quantitatively connect it with coherent K-to-K' valley transport, which moves the electron–hole pairs into a superposition of both valleys contributing opposite helicities to the sideband emission. The ellipticity of the resulting polarisation is a measure of the yield of the intervalley transfer whereas θ is set by the relative phase of the wave functions in the K and the K' valley. Both dynamical and geometric phases contribute. In the future, the delicate variations in the polarization direction of different orders may be quantitatively evaluated to extract geometric phases acquired during lightwave acceleration within the bands.

To visualize the intervalley transport, we calculate the full two-dimensional distribution of the coherent electron–hole polarization $p_{\mathbf{k}}$ in reciprocal space, which is proportional to the density of coherent electron–hole pairs (see Methods). At a zero-crossing of the field, the electrons and holes reside in the K valley (Fig. 4c) while the following half cycle accelerates the leading edge of $p_{\mathbf{k}}$ into the K' valley within a few femtoseconds (Fig. 4d), attesting to subcycle coherent intervalley transport. The distribution function shows major spreading and deformation from the single-peak excitonic packet, mainly due to ionization-induced deformation of the wave packet, whereas a peak close to K is caused by the continued optical excitation during the THz acceleration.

A key question is how far intervalley transport may be ultimately driven. For a realistic scenario, we compute the distribution of $p_{\mathbf{k}}$ for a THz peak field of 23 MV cm^{-1} and a shorter 5-fs near-infrared pulse to prepare electron–hole pairs at a well-defined phase of the THz carrier wave. Figure 4e shows the coherent distribution at its maximal displacement, when the THz field has passed an intense half cycle. Almost the complete distribution of coherent electron–hole pairs (96%) is driven into the K' valley. Here, the time-evolution of the quantum mechanical wave function is effectively inverted by adiabatically shifting it through a time-reversal invariant momentum point. These calculations are supported by a first experiment that utilizes subcycle injection with a 10-fs optical pulse and transfers 66% of the coherent electron–hole pairs into the K' valley (see Extended Data Figure 2). We anticipate that custom-tailored THz waveforms and injection times could allow for more sophisticated transfer protocols yet, paving the way to ultimately fast valleytronics.

Methods

Experimental set-up

A femtosecond titanium-sapphire laser amplifier (repetition rate, 3 kHz; pulse energy, 5.5 mJ; pulse duration, 33 fs; centre wavelength, 805 nm) pumps two parallel dual-stage optical parametric amplifiers (OPA) delivering signal pulses with energies of up to 0.5 mJ and

centre wavelengths that are tuneable between 1.1 and 1.6 μm. We generate intense, phase-locked waveforms in the far- to mid-infrared spectral region (multi-terahertz range) via difference frequency generation between the spectrally detuned phase-correlated near-infrared pulse trains of the OPA. The electric peak field of these few-cycle pulses reaches values of up to 1 V Å^{-1}. A YAG-based (yttrium aluminium garnet) super-continuum source provides ultrabroadband excitation pulses, covering the near-infrared and visible spectral range. The excitation pulse and the THz driving field are superimposed with an indium-tin-oxide-coated beam splitter and are collinearly focused onto a tungsten diselenide sample by a gold-coated parabolic mirror. The full-width-at-half-maximum (FWHM) spot sizes of the excitation pulse and the THz transient at the sample position are 22 μm and 50 μm (intensity FWHM), respectively. For our experiments, the centre frequency of the THz driving field is set to $\nu_{THz} = 40$ THz, while the peak electric field in air amounts to $E_{THz} = 18$ MV cm^{-1} unless stated otherwise. With the help of a mechanical delay stage in the excitation beam path, the temporal overlap of both pulses is adjusted for maximum sideband emission. For a resonant excitation of the excitonic 1s ground state (photon energy, 1.621 eV for the bulk and 1.665 eV for the monolayer) in WSe$_2$ kept at room temperature, optical band-pass filters with a bandwidth of 10 nm are employed to spectrally constrain the white-light pulses. The generated high-order sideband radiation is recorded with a spectrograph coupled to a thermoelectrically cooled silicon charge-coupled device (CCD) camera. All spectra are corrected for the diffraction efficiency of the grating and the quantum efficiency of the detector as well as the sensitivity of the spectrograph for different polarizations. For the valley-selective injection of electron–hole pairs with σ_+-polarized light, we employ a combination of a half-wave and a quarter-wave plate in the beam path of the white-light pulses. The polarization states of the excitation pulses and the emitted sidebands are analysed by a Glan-Thompson polarizer (extinction ratio, 10^{-5}) placed after the sample. Employing ultrashort gating pulses (pulse duration, 10 fs), we detect the waveform of the THz transients by electro-optic sampling in a 6.5-μm-thick zinc telluride crystal while accounting for the detector response[31].

Sample preparation

Bulk-like and monolayer samples of tungsten diselenide are mechanically exfoliated from a bulk crystal onto an intermediate substrate, a visco-elastic gel film (PDMS, Extended Data Figure 1b). There, the sample thickness is verified using optical contrast. Subsequently, the samples are transferred to a CVD-grown (chemical vapour deposition) diamond substrate (Extended Data Figure 1c). In this dielectric environment, the exciton binding energy amounts to 0.25 eV (ref. 32), corresponding to a Keldysh parameter of 0.16 for the field ionization of the exciton using a THz amplitude of 18 MV cm^{-1}. The energy of the 1s A exciton state is confirmed by absorption measurements employing the white light pulses as well as photoluminescence emission under continuous-wave excitation of a green laser diode operating at a wavelength of 533 nm. All experiments are performed under ambient conditions. The crystal orientation is determined by second-harmonic generation. For this purpose, linearly polarized, 10-fs near-infrared pulses are focused onto the monolayer sample. The second-harmonic intensity with a polarization parallel to the fundamental, $I_{SHG,\parallel}$, is monitored using a spectrograph with a cooled silicon CCD. $I_{SHG,\parallel}$ peaks in the armchair direction (Extended Data Figure 1a), where inversion symmetry is explicitly

broken in the real space lattice (compare Fig. 1a). Since monolayer WSe_2 preferably cleaves along high-symmetry directions, the alignment procedure is complemented by optical microscope images (Extended Data Figure 1b and c). We estimate that the crystal orientation is determined with an uncertainty of approximately $\pm 1°$.

Density functional theory calculations

Our DFT calculations are performed with a full-potential linearized augmented plane-wave all-electron method as implemented in the Wien2k code[33]. Specific calculation parameters and an optimized structure of WSe_2 were taken from ref. 34. The wave function (muffin-tin radii, 2.46 and 2.34 atomic units for W and Se, respectively) was expanded in partial waves with orbital quantum numbers up to 10. For the interstitial region, we used a plane wave cut-off of 6.5 $Å^{-1}$. The spin-orbit interaction has been included fully relativistically for core electrons while W $5s^2$ $5p^6$ $4f^{14}$ $5d^4$ $6s^2$ and Se $3d^{10}$ $4s^2$ $4p^4$ valence electrons have been treated within a second variational step method[35]. For the exchange-correlation functional, we consider the generalized gradient approximation[36]. These DFT calculations provide the relevant electronic bands and dipole matrix elements (including both σ_+ and σ_- contributions) throughout the irreducible Brillouin zone wedge.

Since DFT solves electronic states and matrix elements from the atomistic level up by using minimal assumptions it is a first-principles approach. Nevertheless, DFT must always approximate the correlation energy functional because its dependence on density still remains unknown. To reproduce the experimental band gap and exciton resonance energies, we adjust both the band gap and dielectric constant of the Coulomb interaction V. We apply the Keldysh form for V to account for the principal aspects of dielectric screening inside a monolayer. These inputs uniquely define both the Coulomb and light–matter interactions needed to systematically describe electron–hole excitations generated by an optical and a THz field. These procedures yield an accurate description of the excitonic features of transition metal dichalcogenides as shown in ref. 37.

Cluster-expansion computations

The cluster-expansion approach solves the many-body problem from the point of view of correlations, as an alternative perspective compared to DFT. Earlier investigations with semiconductors[23], Jaynes-Cummings model[38], and strongly interacting atomic Bose–Einstein condensates[39] show that the many-body dynamics can be cast into a format exactly described in terms of a sequential build-up of clusters. Since the cluster expansion defines all the resulting correlation functionals exactly[40] for any given many-body Hamiltonian, it also is a first-principles approach. The description, furthermore, is non-perturbative in terms of the interaction strength[41,42], which makes it ideally suited for studying extreme nonlinearities created, for example, by high-order sideband generation. Since clusters build up sequentially the dynamics on extremely short times scales are well described by completely omitting clusters beyond a certain level of complexity. This circumstance makes the cluster-expansion computations extremely efficient and accurate in describing ultrafast quantum kinetics of very diverse many-body systems.

Here, the optical field $\mathbf{E}_{opt}(t)$ dominantly excites a coherent superposition between the valence and the conduction band, that is, a microscopic polarization $p_{\mathbf{k}}$. The polarization $p_{\mathbf{k}}$ can be characterized by a single-particle cluster[23,41] describing coherently driven electron–hole pairs at crystal momentum $\hbar\mathbf{k}$. The polarization dynamics form the backbone of the semiconductor Bloch equations (SBEs); its polarization part has the structure

$$i\hbar\frac{\partial}{\partial t}p_{\mathbf{k}} = \epsilon_k p_{\mathbf{k}} - \left(1 - f_{\mathbf{k}}^{e} - f_{-\mathbf{k}}^{h}\right)\Omega_{\mathbf{k}}(t) + i|e|\mathbf{E}_{THz}(t) \cdot \nabla_{\mathbf{k}}p_{\mathbf{k}} + \Gamma_{\mathbf{k}} ,$$

where ϵ_k is the Coulomb-renormalized electron–hole energy (defined by the DFT input), $f_{\mathbf{k}}^{e}\left(f_{\mathbf{k}}^{h}\right)$ is the electron (hole) occupation at $\mathbf{k}$, $\Omega_{\mathbf{k}}(t) = \mathbf{d}_{\mathbf{k}} \cdot \mathbf{E}_{opt}(t) + \Sigma_{\mathbf{k}}{}' \, V_{\mathbf{k}}{}'_{-\mathbf{k}} \, p_{\mathbf{k}}{}'$ is the Rabi energy renormalized by the Coulomb interaction $V_{\mathbf{k}}$. Both $V_{\mathbf{k}}$ and the dipole-matrix element $\mathbf{d}_{\mathbf{k}}$ are defined from DFT. Once the optical field $\mathbf{E}_{opt}(t)$ generates the polarization, the THz field $\mathbf{E}_{THz}(t)$ accelerates it via the gradient term. The generated microscopic polarization also scatters with densities and other polarization $p_{\mathbf{k}}$ due to Coulomb interaction, inducing a two-particle correlation $\Gamma_{\mathbf{k}}$ that introduces exciton-state dependent dephasing for polarization. This full microscopic scattering is included using the description of ref. 43. This yields a fully microscopic description of exciton-state dependent dephasing, which considerably decreases the coherence time for all other excitons than the 1s state[41]. This level of sophistication is necessary to systematically model the decay of coherent electron–hole pairs during their life cycle encompassing preparation, acceleration, and recollision. Since TMDC monolayers couple strongly to light, we also include the self-consistent coupling of the SBEs with Maxwell's equations following the exact approach of ref. 41 using the experimental geometry vacuum–monolayer–diamond–vacuum. This allows us to predict both transmitted and reflected fields in absolute units, as well as to include the radiative decay to the analysis. We use the DFT material parameters and matrix elements as an input to solve the full two-dimensional quantum polarization kinetics using 170 radial wave vectors spanning the full Brillouin zone and 241 angular states.

HSG and symmetry

Broken inversion symmetry is a necessary requirement for odd-order sideband generation. Inversion symmetric media, such as bulk crystals of silicon or diamond, do not facilitate odd-order HSG. Broken out-of-plane symmetry at surfaces, interfaces and two-dimensional materials can manifest itself only if the driving field has a strong out-of-plane component. As seen in Fig. 1c, the strongest effect of HSG occurs in crystal directions in which the symmetry of the band structure rather than the symmetry of the real-space lattice is broken. This scenario is caused by the fact that HSG originates from intraband currents. Interestingly, the third-order sideband in Fig. 1c is relatively strongly suppressed. This feature is indeed expected (Fig. 2) since this sideband results from electron–hole excursions that barely reach the asymmetric band structure features whereas higher-order sidebands are associated with substantially longer trajectories in $\mathbf{k}$ space. Nonetheless, even in cases where the band structure is asymmetric, odd-order HSG may require an additional condition. Our experiment with linearly polarized excitation light exemplifies the situation. Since the band structure is mirror symmetric with respect to the M point, the intraband dynamics of electron–hole pairs in the K valley driven by a positive THz field are identical to the

intraband dynamics of electron–hole pairs in the K' valley driven by a sign-inverted THz field. For equal population of both valleys, the total system may seem inversion symmetric at first glance. The observation of odd-order HSG (Fig. 1c, red curve) can be explained only if the valley pseudospin is taken into account: Electron–hole recollisions from different valleys are disentangled by the valley-specific helicity of the emitted light. Alternatively, the contributions of both valleys can be separated by exciting only one valley with circularly polarized light (Fig. 4a). In any case, the emergence of odd-order sidebands in monolayer WSe$_2$ is a direct consequence of the valley pseudospin in the material. We further underpin the influence of the valley pseudospin and intervalley transfer by a first experiment utilizing subcycle injection of coherent electron–hole pairs by a 10-fs pulse (Extended Data Figure 2). We extract a transfer rate of 66% marking the first subcycle transport of internal quantum attributes, which could inspire a development of corresponding quantum logic operations similar to spintronics[44].

Analytical derivation of the high-order sideband polarization for linearly polarized excitation

The theoretical and experimental finding of cross-polarized even and odd sideband orders in the case of a linearly polarized interband excitation (see Fig. 3) is a direct consequence of the opposite pseudospins of the K and K' valleys and can be derived analytically: Due to the optical selection rules of monolayer WSe$_2$, radiative electron–hole recombination in the two valleys generates light of opposite helicity. Consequently, the total emitted field of high-order sidebands $\mathbf{E}_{\mathrm{HSG}}$ consists of contributions from the K and K' valley with right- ($\boldsymbol{\sigma}_+$) and left-circularly polarized light ($\boldsymbol{\sigma}_-$), respectively, and can be written

$$\mathbf{E}_{\mathrm{HSG}} = E_{\mathrm{HSG,K}}\,\boldsymbol{\sigma}_+ + E_{\mathrm{HSG,K'}}\,\boldsymbol{\sigma}_- ,$$

where $E_{\mathrm{HSG,K}}$ and $E_{\mathrm{HSG,K'}}$ denote the contributions from the K and the K' valley, respectively. Owing to the symmetry of the band structure (see Fig. 2a), the dynamics occurring in the K' valley for positive fields of the driving waveform E_{THz} are identical to the dynamics of the K valley for negative fields (K and K' points are time reversal pairs). Hence, we can substitute $E_{\mathrm{HSG,K'}}(E_{\mathrm{THz}})$ with $E_{\mathrm{HSG,K}}(-E_{\mathrm{THz}})$. By simultaneously exploiting the relation that $\boldsymbol{\sigma}_\pm = \left(\mathbf{e}_x \mp i\mathbf{e}_y\right)/\sqrt{2}$, with the Cartesian unit vectors $\mathbf{e}_x$ and $\mathbf{e}_y$, we can rewrite the above relation:

$$\mathbf{E}_{\mathrm{HSG}} = E_{\mathrm{HSG,K}}(E_{\mathrm{THz}})(\mathbf{e}_x - i\mathbf{e}_y)/\sqrt{2} + E_{\mathrm{HSG,K}}(-E_{\mathrm{THz}})(\mathbf{e}_x + i\mathbf{e}_y)/\sqrt{2} .$$

Furthermore, one can decompose $E_{\mathrm{HSG,K}}$ into even- and odd-order contributions, that is, $E_{\mathrm{HSG,K}} = E_{\mathrm{even}} + E_{\mathrm{odd}}$. Since only even (odd) powers of E_{THz} contribute to E_{even} (E_{odd}), these fields feature even (odd) parity with respect to the THz driving field. Taking these relations into account, one can state

$$E_{\mathrm{HSG,K}}\!\left(\pm E_{\mathrm{THz}}\right) = E_{\mathrm{even}} \pm E_{\mathrm{odd}},$$

and we arrive at:

$$\mathbf{E}_{\text{HSG}} = \left(E_{\text{even}} + E_{\text{odd}}\right)\left(\mathbf{e}_{\text{x}} - i\mathbf{e}_{\text{y}}\right)/\sqrt{2} + \left(E_{\text{even}} - E_{\text{odd}}\right)\left(\mathbf{e}_{\text{x}} - i\mathbf{e}_{\text{y}}\right)/\sqrt{2},$$

$$\mathbf{E}_{\text{HSG}} \propto E_{\text{even}} \cdot \mathbf{e}_{\text{x}} - E_{\text{odd}} \cdot i\mathbf{e}_{\text{y}}.$$

Consequently, the conserved circular dichroism directly leads to cross polarized even and odd orders. These derivations still hold for large intervalley transfer as long as the optical selection rules hold. Our experimental observations confirm this fact as well as the conservation of the valley coherence during lightwave acceleration.

Extended Data
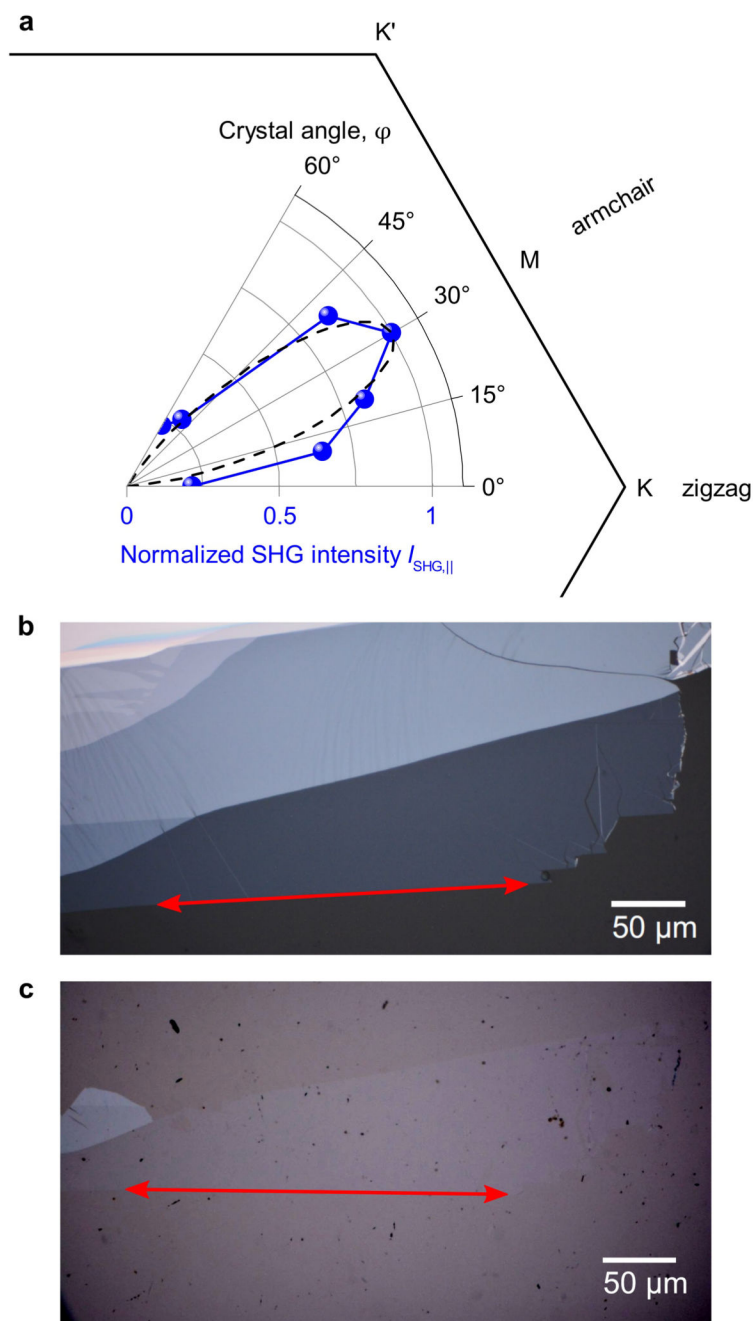
Extended Data Figure 1. Sample orientation.
a, Azimuthal scan of the second harmonic intensity polarized parallel to the excitation pulse, $I_{SHG,\parallel}$ (blue curve), revealing the armchair direction at an crystal angle of $\varphi = 30°$. The dashed line marks the expected scaling proportional to $\sin^2(3\varphi)$. Around the polar diagram, the hexagonal Brillouin zone of WSe_2 is depicted with the high-symmetry points. **b,** Optical microscope image of the exfoliated monolayer on the visco-elastic gel film used for

exfoliation. Areas appearing in lighter grey are few-layer tungsten diselenide. **c,** Monolayer sample after transfer to a diamond substrate. The contrast of this image has been enhanced to improve the visibility of the atomically thin WSe$_2$ film. The red arrows mark the same edge in **b** and **c**, which has been identified as the zigzag direction using the SHG scan.
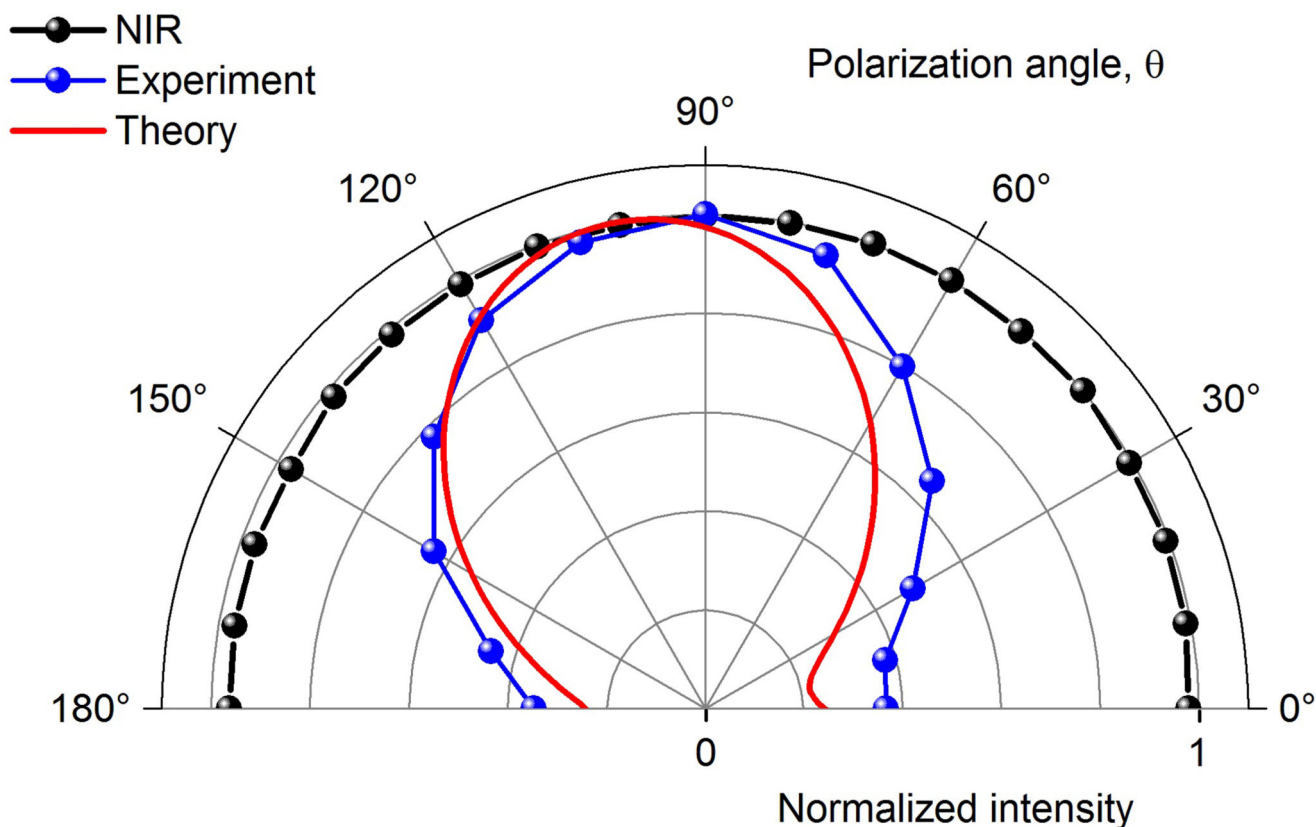
Extended Data Figure 2. Polarization of subcycle sideband emission.
Circularly polarized 10-fs near-infrared pulses (polarization-resolved intensity depicted as black spheres) excite valley-polarized electron–hole pairs in a monolayer of tungsten diselenide. Simultaneously, an atomically strong THz wave is applied in the zigzag direction and may transfer electrons and holes to the non-excited K' valley. The high-order sideband emission resulting from coherent electron–hole collisions driven by the most intense half cycle is measured to have an elliptical polarization (blue spheres), containing contributions from the opposite valley. Our quantum theory reproduces this polarization state (red curve) and reveals a transfer yield of 66% to the initially unexcited K' valley.

Acknowledgements

References

1. Markov IL. Limits on fundamental limits to computation. Nature. 2014; 512:147–154. [PubMed: 25119233]

2. Ladd TD, et al. Quantum computers. Nature. 2010; 464:45–53. [PubMed: 20203602]

3. Krausz F, Stockman MI. Attosecond metrology: from electron capture to future signal processing. Nat Photon. 2014; 8:205–213.

4. Corkum PB, Krausz F. Attosecond science. Nat Phys. 2007; 3:381–387.

5. Ghimire S, et al. Observation of high-order harmonic generation in a bulk crystal. Nat Phys. 2011; 7:138–141.

6. Zaks B, Liu RB, Sherwin MS. Experimental observation of electron–hole recollisions. Nature. 2012; 483:580–583. [PubMed: 22460904]

7. Schubert O, et al. Sub-cycle control of terahertz high-harmonic generation by dynamical Bloch oscillations. Nat Photon. 2014; 8:119–123.

8. Hohenleutner M, et al. Real-time observation of interfering crystal electrons in high-harmonic generation. Nature. 2015; 523:572–575. [PubMed: 26223624]

9. Higuchi T, Heide C, Ullman K, Weber HB, Hommelhoff P. Light-field-driven currents in graphene. Nature. 2017; 550:224–228. [PubMed: 28953882]

10. Vampa G, et al. Linking high-harmonics from gases and solids. Nature. 2015; 522:462–464. [PubMed: 26108855]

11. Garg M, et al. Multi-petahertz electronic metrology. Nature. 2016; 538:359–363. [PubMed: 27762353]

12. Langer F, et al. Lightwave-driven quasiparticle collisions on a subcycle timescale. Nature. 2016; 533:225–229. [PubMed: 27172045]

13. Liu H, et al. High-harmonic generation from an atomically thin semiconductor. Nat Phys. 2017; 13:262–266.

14. Yoshikawa N, Tamaya T, Tanaka K. High-harmonic generation in graphene enhanced by elliptically polarized light excitation. Science. 2017; 356:736–738. [PubMed: 28522530]

15. Sivis M, et al. Tailored semiconductors for high-harmonic optoelectronics. Science. 2017; 357:303–306. [PubMed: 28729510]

16. Wolf SA, et al. Spintronics: A Spin-Based Electronics Vision for the Future. Science. 2001; 294:1488–1495. [PubMed: 11711666]

17. Schaibley JR, et al. Valleytronics in 2D materials. Nat Rev Mat. 2016; 1 16055.

18. Xu X, Wang Y, Xiao D, Heinz TF. Spin and pseudospins in layered transition metal dichalcogenides. Nat Phys. 2014; 10:343–350.

19. Xiao D, Liu G-B, Feng W, Xu X, Yao W. Coupled Spin and Valley Physics in Monolayers of MoS_2 and Other Group-VI Dichalcogenides. Phys Rev Lett. 2012; 108 196802.

20. Aivazian G, et al. Magnetic control of valley pseudospin in monolayer WSe_2. Nat Phys. 2015; 11:148–152.

21. Ye Z, Sun D, Heinz TF. Optical manipulation of valley pseudospin. Nat Phys. 2017; 13:26–29.

22. Bloch F. Über die Quantenmechanik der Elektronen in Kristallgittern. Z Phys. 1928; 52:555–600.

23. Kira M, Koch SW. Semiconductor Quantum Optics. Cambridge University Press; Cambridge: 2012.

24. Yan J-Y. Theory of excitonic high-order sideband generation in semiconductors under a strong terahertz field. Phys Rev B. 2008; 78 075204.

25. Vampa G, et al. All-Optical Reconstruction of Crystal Band Structure. Phys Rev Lett. 2015; 115 193603.

26. Banks HB, et al. Dynamical Birefringence: Electron–Hole Recollisions as Probes of Berry Curvature. Phys Rev X. 2017; 7 041042.

27. Mak KF, He K, Shan J, Heinz TF. Control of valley polarization in monolayer MoS_2 by optical helicity. Nat Nanotech. 2012; 7:494–498.

28. Jones AM, et al. Optical generation of excitonic valley coherence in monolayer WSe$_2$. Nat Nanotech. 2013; 8:634–638.

29. Wang G, et al. Control of Exciton Valley Coherence in Transition Metal Dichalcogenide Monolayers. Phys Rev Lett. 2016; 117 187401.

30. Rycerz A, Tworzydło J, Beenakker CWJ. Valley filter and valley valve in graphene. Nature Phys. 2007; 3:172–175.

31. Gallot G, Grischkowsky D. Electro-optic detection of terahertz radiation. J Opt Soc Am B. 1999; 16:1204–1212.

32. Poellmann C, et al. Resonant internal quantum transitions and femtosecond radiative decay of excitons in monolayer WSe$_2$. Nat Mater. 2015; 14:889–893. [PubMed: 26168345]

33. Blaha P, Schwarz K, Madsen GKH, Kvasnicka D, Luitz J. Wien2k, An Augmented Plane Wave + Local Orbitals Program for Calculating Crystal Properties. Vienna: University of Technology; 2013.

34. Kormányos A, et al. k·p theory for two-dimensional transition metal dichalcogenide semiconductors. 2D Mater. 2015; 2 022001.

35. Singh DJ, Nordström L. Planewaves, Pseudopotentials, and the LAPW Method. Springer; New York: 2006.

36. Perdew JP, Burke K, Ernzerhof M. Generalized Gradient Approximation Made Simple. Phys Rev Lett. 1996; 77:3865. [PubMed: 10062328]

37. Steinhoff A, Rösner M, Jahnke F, Wehling TO, Gies C. Influence of Excited Carriers on the Optical and Electronic Properties of MoS$_2$. Nano Lett. 2014; 14:3743–3748. [PubMed: 24956358]

38. Mootz M, Kira M, Koch SW. Sequential build-up of quantum-optical correlations. J Opt Soc Am B. 2012; 29:A17–A24.

39. Kira M. Hyperbolic Bloch equations: Atom-cluster kinetics of an interacting Bose gas. Ann Phys. 2015; 356:185–243.

40. Mootz M, Kira M, Koch SW. Pair-excitation energetics of highly correlated many-body states. New J Phys. 2013; 15 093040.

41. Kira M, Koch SW. Many-body correlations and excitonic effects in semiconductor spectroscopy. Prog Quantum Electron. 2006; 30:155–296.

42. Kira M. Coherent quantum depletion of an interacting atom condensate. Nat Commun. 2015; 6:6624. [PubMed: 25767044]

43. Smith RP, et al. Extraction of Many-Body Configurations from Nonlinear Absorption in Semiconductor Quantum Wells. Phys Rev Lett. 2010; 104 247401.

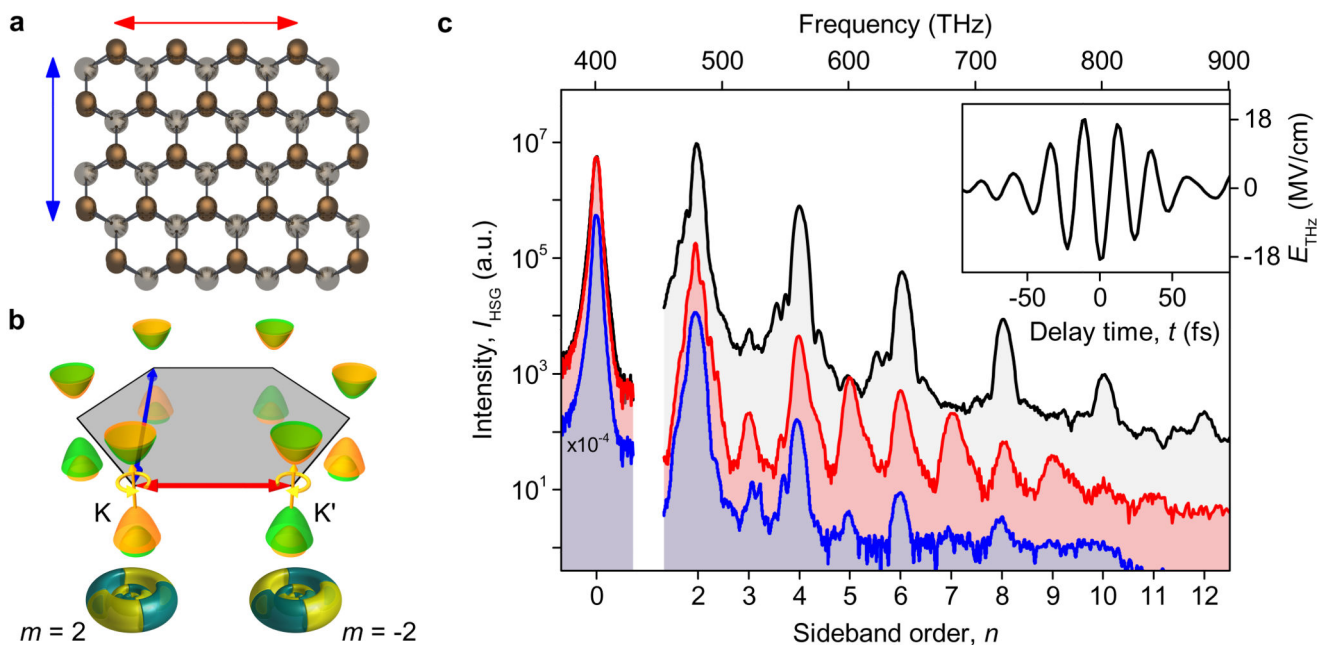44. Loss D, DiVincenzo DP. Quantum computation with quantum dots. Phys Rev A. 1998; 57:120–126.

Figure 1. High odd-order sideband generation in monolayer WSe₂.
a, Crystal structure of a WSe_2 monolayer. Tungsten atoms are depicted as grey, selenium atoms as brown spheres. **b,** Hexagonal Brillouin zone with the spin-split valence and conduction band edges at the inequivalent K and K' points. The main orbital contributions to the top of the valence bands as calculated from DFT are shown below (green-yellow colour scale depicts the sign of the imaginary part). Red (blue) arrows in **a** and **b** indicate the zigzag (armchair) direction. **c,** High-order sideband intensity I_{HSG} measured from bulk WSe_2 (black) and monolayer WSe_2 in the zigzag (red) and the armchair direction (blue, shifted downwards by one order of magnitude for a better visibility). In the zigzag direction, even- and odd-order sidebands exhibit comparable intensities, while odd orders are almost completely suppressed in the armchair direction. Note, that the frequency axis of the bulk spectrum has been shifted by 9 THz owing to the different excitation frequencies. Inset: electro-optically sampled multi-THz field, featuring a frequency of $\nu_{THz} = 40$ THz and a peak field strength in air of $E_{THz} = 18$ MV cm^{-1}.

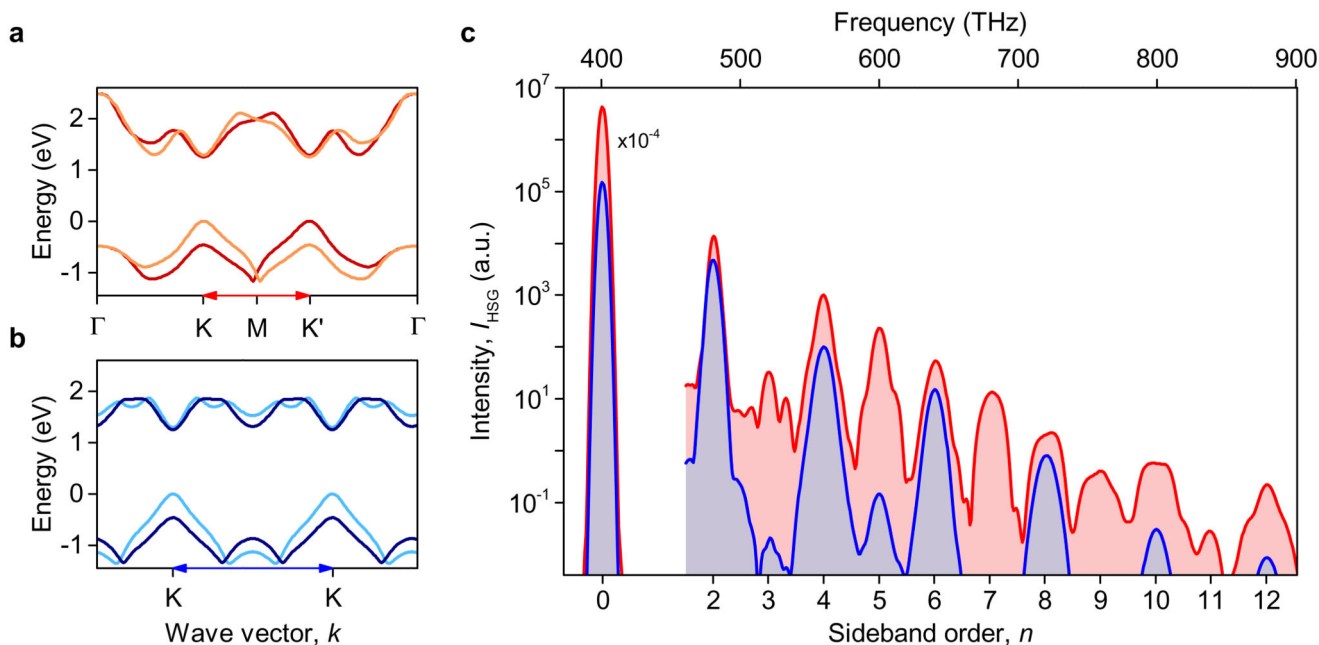**Figure 2. Electronic structure of WSe$_2$ and quantum theory of high-order sideband generation.**
a,b, Band structure of monolayer WSe$_2$ calculated by DFT for the zigzag (**a**) and the armchair direction (**b**) (dark colours, spin-up; light colours, spin-down bands). There is no inversion symmetry about the K/K' valleys in the zigzag direction, supporting the generation of odd-order sidebands. The bands in the armchair direction are inversion symmetric inhibiting odd-order HSG. The red and blue arrows at the bottom of each panel indicate the high-symmetry directions highlighted in Fig. 1. **c,** Computed intensity spectrum I_{HSG} for lightwave-driven electron–hole recollision along the zigzag (red) and armchair (blue, shifted along the intensity axis by one order of magnitude for better visibility) directions.
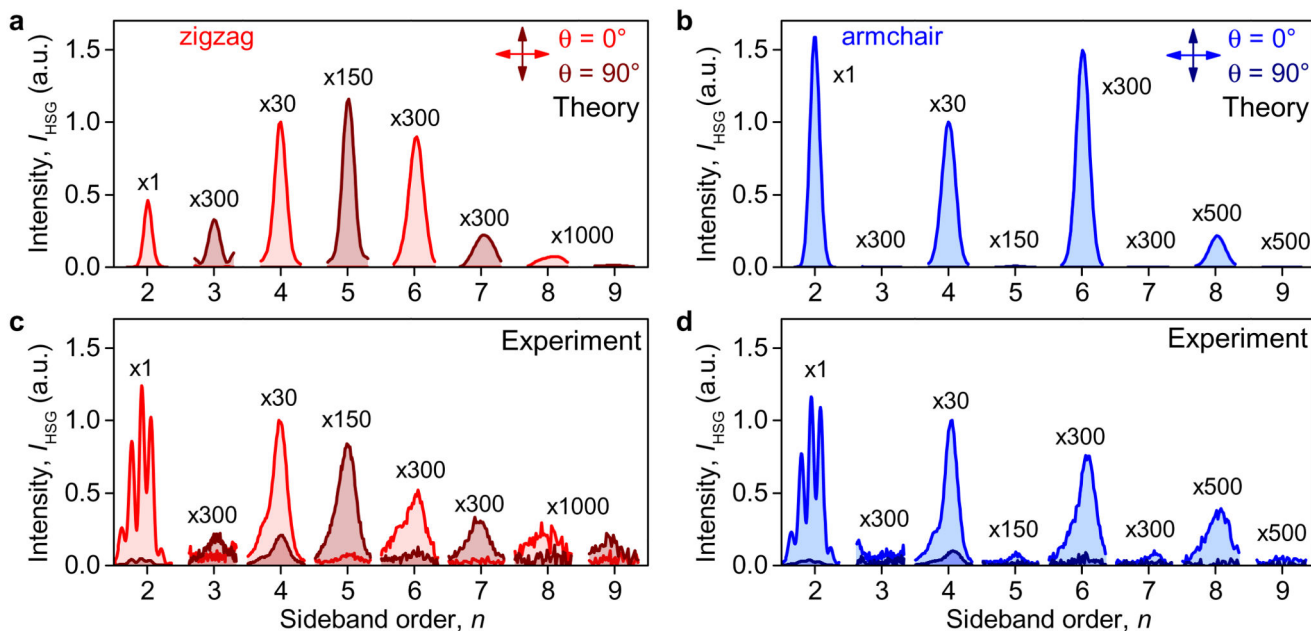
Figure 3. High-order sideband polarization for different crystal orientations.
a,b, Simulated high-order sideband intensity in the polarization basis parallel ($\theta = 0°$, light colours) and perpendicular ($\theta = 90°$, dark colours) to the linearly polarized excitation and driving fields, taking into account the polarization contributions of opposite helicity in the different valleys. Individual sideband orders are multiplied with the indicated multiplication factors. Even and odd orders are cross-polarized in the zigzag direction (**a**), while the armchair direction (**b**) only supports strong even orders with a parallel polarization. **c,d,** Measured polarization-resolved intensity I_{HSG} normalized to the fourth order for a multi-THz field pointing along the zigzag (**c**) and the armchair (**d**) direction. The zigzag direction confirms cross-polarized even- and odd-order sidebands, while all orders in the armchair direction exhibit a parallel polarization (odd orders suppressed by crystal symmetry).
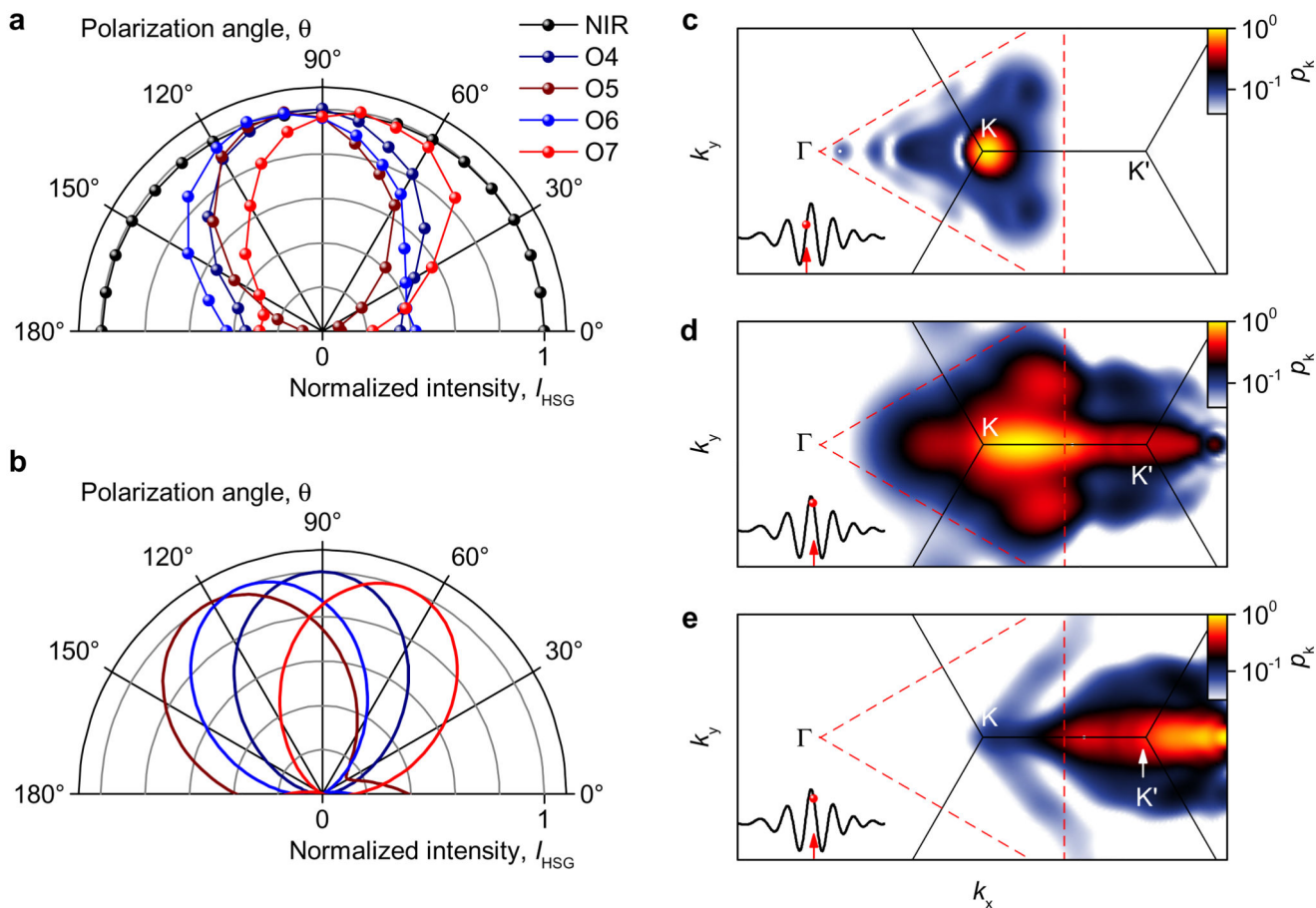
Figure 4. Intervalley mixing and lightwave valleytronics.
a, Measured polarization-resolved intensity I_{HSG} of individual sideband orders (normalized, coloured data points) for circularly polarized excitation (normalized, black data points) of the K valley only. The THz-driven intraband transport ($E_{THz} = 23$ MV cm^{-1}, along the zigzag direction) into the K' valley adds polarization contributions of opposite helicity resulting in an overall elliptical polarization. **b,** Computed polarization of high-order sidebands (orders four to seven, solid lines, same colours as in **a** following a valley-selective excitation in the K valley. **c,d,** Computed distribution of the coherent electron–hole polarization p_k (colour scale) in reciprocal space at the time of small (**c**) and maximal displacement (**d**); conditions match the experimental analysis in **a**. Near a zero-crossing of the electric field (indicated in the inset of **c**) the coherent electron–hole pairs reside in the K valley (borders indicated by red dashed lines). In the following half cycle (**d**), a pronounced ledge of electrons and holes is driven from the K to the K' valley, underpinning subcycle valley transport. **e,** Computed polarization following a subcycle excitation by a 5-fs optical pulse and THz acceleration by an electric field of 23 MV cm^{-1}. The maximum of the polarization is transferred far into the K' valley, demonstrating that the valley pseudospin can indeed be switched by strong THz fields.